Paper II

Probing cold dark matter subhalos with simulated ALMA observations of macrolensed sub–mm galaxies

Saghar Asadi,[1]* Erik Zackrisson,[2] Emily Freeland[1]

[1] *Department of Astronomy, Stockholm University, Oscar Klein Center, AlbaNova, Stockholm SE–106 91, Sweden*
[2] *Department of Physics and Astronomy, Uppsala University, Box 515, SE–751 20 Uppsala, Sweden*

ABSTRACT
If the dark matter halos of galaxies contain large numbers of subhalos as predicted by the ΛCDM model, these subhalos are expected to appear in strong galaxy–galaxy lens systems as small–scale perturbations in individual images. We simulate observations of multiply–lensed sub–mm galaxies at $z \sim 2$ as a probe of the dark matter halo of a lens galaxy at $z \sim 0.5$. We present detection limits for dark substructures based on a visibility plane analysis of simulated ALMA data in bands 7, 8 and 9. This method benefits from the use of complex visibilities to put emphasis on different angular scales via the choice of the weighting scheme. We explore two effects: a local surface brightness deflection on angular scales similar to the Einstein radius and the astrometric shift of the image. This improves the sensitivity of our lens modeling to the mass of the lens perturber. We stress that this technique is more sensitive to detection of low–mass subhalos compared to other techniques which use image plane modeling. We demonstrate that pseudo-Jaffe subhalos can be detected with 99% confidence down to masses of $\approx 3 \times 10^7 M_\odot$ in ALMA band 7, $\approx 5 \times 10^7 M_\odot$ in band 8 and $\approx 8 \times 10^7 M_\odot$ in band 9. However, the mass and the shape parameter of Einasto subhalos remain highly degenerate.

Key words: techniques: interferometric – gravitational lensing: strong – galaxies: dwarf – radio continuum: galaxies – submillimetre: galaxies – dark matter

1 INTRODUCTION

Cosmological N–body simulations predict the existence of dark matter halos in the mass range from galaxy cluster halos ($\sim 10^{15} M_\odot$) down to the smallest halos corresponding to the cutoff in the primordial matter power spectrum. The high–mass end of the halo mass function can be tested through anisotropies in the cosmic microwave background radiation (e.g. Wright et al. 1992; Bennett et al. 2013; Planck Collaboration et al. 2014), and the low–mass end is highly dependent on the detailed properties of dark matter particles; particularly particle mass and decoupling velocity (e.g. Bertone, Hooper, & Silk 2005). The cutoff mass constraint varies widely from one particle candidate to another. WIMP models usually suggest a minimum halo mass as low as $\sim 10^{-11} M_\odot$ for light dark matter particles (e.g. Bringmann 2009; Cornell, Profumo, & Shepherd 2013).

Dark matter–only cosmological N–body simulations assume the gravitational interaction between WIMPs to be the dominant driving force of structure formation (see for instance Springel et al. 2008; Gao et al. 2012; Schaller et al.

2015, for projects Aquarius, Phoenix, and EAGLE, respectively). As a result, dark matter halos that host galaxies form in a hierarchical process during which small halos that are bound to the gravitational potential of a massive halo join the smooth matter content of the parent halo through tidal disruption. This gradual process takes up to several billion years to complete. During this hierarchical assembly, smaller halos tend to stay present within the parent halo in the form of a clumpy substructure on top of the smooth matter distribution. A generic prediction of dark matter–only simulations is that $\sim 10\%$ of the total halo mass of a galaxy at $z = 0$ is in the form of a clumpy structure bound to the smooth halo (Gao et al. 2008; Maciejewski et al. 2011). These subhalos of simulated galaxy–sized CDM halos are best–fitted by a mass function of the type:

$$\frac{\mathrm{d}N}{\mathrm{d}M} \propto M^{-\alpha}$$

with $\alpha \approx 1.9$ (Springel et al. 2008; Gao et al. 2008, 2012; Xu et al. 2012) at the low–mass end, resulting in simulated dark halos that greatly outnumber the dwarf satellites of Milky Way and Andromeda (see e.g. Klypin et al. 1999; Moore et al. 1999).

* E-mail: saghar.asadi@astro.su.se (SA)

A recent challenge for ΛCDM at small–scales is the mismatch between the most massive subhalos at $z = 0$ in simulations and the most massive satellite galaxies in the local group, the so–called "too big to fail" problem (Boylan-Kolchin, Bullock, & Kaplinghat 2011, 2012). In the absence of full hydrodynamic cosmological simulations, adopting baryonic physics and feedback processes in simulations on galaxy/group scales seems to be able to regulate both the local group dwarf population with respect to that of dark matter halos and the correspondence between the most massive halos and satellites (e.g. Garrison-Kimmel et al. 2014; Sawala et al. 2014; Fry et al. 2015; Schaller et al. 2015). Adopting non–standard properties for dark matter particles also provides a competitive, and maybe complimentary, solution to both these discrepancies (e.g. Lovell et al. 2012; Vogelsberger, Zavala, & Loeb 2012; Wang et al. 2014).

Simulated dark matter halos generally fit to a universal 3D density profile increasing towards the center as $\rho \propto r^{-\alpha}$, $\alpha = 1$ (shallower than an isothermal sphere with $\alpha = 2$), while the logarithmic slope decreases at larger radii, i.e. $\alpha = 3$ for $r > r_s$ (Navarro, Frenk, & White 1996). Observationally, dwarf and low surface brightness galaxies show flat dark matter mass density profiles in the center, i.e. $\alpha = 0$ (e.g. Moore 1994; Zackrisson et al. 2006; Kuzio de Naray 2008; Oh et al. 2011; Kuzio de Naray & Spekkens 2011; de Blok 2010; Walker & Peñarrubia 2011; Amorisco & Evans 2012). Baryonic feedback processes may be responsible for the "cored" central density profiles in baryon–dominated regions (see e.g. Navarro, Eke, & Frenk 1996; de Blok et al. 2001; Maxwell, Wadsley, & Couchman 2015). However, dark matter–dominated halos seem to be following a nearly universal density profile which is much "cuspier" in the center.

Gravitational lensing as a probe of dark halo substructures places constraints on the low–mass end of the dark matter halo mass function (for a review see Zackrisson & Riehm 2010) at $z > 0$. Even though the surface brightness is conserved in gravitational lensing, the angular size and integrated flux of the lensed object are magnified. This can be used as a tool for resolving high–redshift background objects such as sub–mm galaxies (Hezaveh et al. 2013).

The strong lensing effect requires a close alignment of the source, the lens, and the observer to result in multiple lensed images of the back ground source. The total mass content of the foreground lens, including both the underlying smooth dark matter halo and the substructure, is probed by studying locations and relative fluxes of these macroimages. Observations have attempted to constrain the contribution from dark matter substructure using two techniques : the statistical examination of flux ratio anomalies and compound lensing of single perturbers.

While simple, smooth models of lens galaxies are usually able to reproduce the positions of the macroimages, their observed flux ratios are more difficult to understand. These flux–ratio anomalies have been interpreted as evidence of substantial small–scale structure within the main lens (e.g. Chiba 2002; Keeton 2003; Kochanek & Dalal 2004; Cyr-Racine et al. 2015). They provide statistical constraints on the mass fraction of galactic halos in the form of substructure and possibly the mass function of the subhalos. Inferred values of the projected subhalo mass fraction vary between $f_{sub} \approx 0.002$ (Xu et al. 2009) from flux ratio anomalies, to $f_{sub} \approx 0.006$ (Vegetti et al. 2014) based on gravitational detection of single high–mass subhalos. However, CDM substructure is unlikely to be the only cause of these flux ratio anomalies which implies that this fraction could be considered as an upper limit (see e.g. Xu et al. 2015, for investigating two classes of such contributions; interstellar propagation effects and the use of improper models for the main lens that are either too simple or unrealistic).

The compound lensing technique, on the other hand, is not only able to detect individual subhalos but also to constrain the mass and details of the internal density profile of the subhalo aligned as a perturber in the strong galaxy–galaxy lensing system and consequently different dark matter models. The inferred CDM fraction from strong lensing made by single perturbers indicates a higher fraction (mean projected substructure mass fraction $f = 0.0064$ to $f = 0.0076$ depending on the prior assumptions) of substructure contribution in the surface mass density of a galactic halo (Vegetti et al. 2012, 2014). While methods based on surface brightness perturbation are significantly less sensitive to low–mass halos, flux ratio anomalies are produced by the combination of both low– and high–mass subhalos and due to the exponential decrease of subhalo numbers with increasing mass, massive subhalo alignment becomes increasingly more rare. Therefore, flux ratio anomaly method probes subhalos with $M_{sub} \sim 10^5 M_\odot$, while direct lens perturbers accounted for in Vegetti et al. (2014) are much more massive $M_{sub} \sim 10^8 - 10^9 M_\odot$.

In the next section, we will discuss the two different groups of empirical halo density profiles. Section 3, elaborates on the details of our simulations, including the choices of sources and perturbers and the use of complex visibilities, in comparison to image plane modeling. Our results are presented in section 4, and finally section 5 discusses the results of this work in the context of the field as well as the limitations. A summary of the results can be found in section 6

2   DIFFERENT FORMS OF HALO SUBSTRUCTURE

The central slope of the density profiles of dark matter halos can be measured both from observational data and fits to halos in N–body simulations. In this regard, the single–parameter (cored) singular isothermal sphere (ellipsoid) profile provides an acceptable lens model for the mean dark matter halo of galaxies. On the other hand, the universal density profiles of field halos in CDM simulations can be reasonably well described by Navarro, Frenk, & White (1996, hereafter NFW) profile:

$$\rho(r) = \frac{\rho_s}{(r/r_s)(1 + r/r_s)^2}$$

where r_s is the characteristic scale radius of the halo, i.e. the radius at which $\rho \propto 1/r^2$, and ρ_s is the density at $r = r_s$. An extra parameter called the *concentration parameter* c relates the scale density of the halo to its virial radius and is defined as $c \equiv r_s/r_{vir}$. The concentration parameter therefore, contains information about the formation and evolution of the halo and depends on the time of

the collapse of the halo as well as its virial mass. Given the hierarchical formation of halos, the low–mass halos were formed at higher redshift where the mean density of the Universe was higher and so was the inner density of collapsed halos. This results in a weak $c - M_{\rm vir}$ correlation such that the concentration parameter decreases with increasing $M_{\rm vir}$. Besides, low–mass subhalos gradually lose mass in tidal interaction with the parent halo which leads to a further increase of their $c_{\rm vir}$ over time (Bullock et al. 2001; Macciò, Dutton, & van den Bosch 2008).

Relaxing the central logarithmic slope $\gamma = \frac{d \ln(\rho/\rho_s)}{d \ln(r/r_s)}$ in the basic two–parameter form of NFW profile makes better fit to individual halos in CDM simulations. In this three–parameter form, the inner cusp slope becomes progressively shallower towards the center, eventually reaching inner slope of $\gamma \geq -1$. The generalized NFW profile (gNFW) is formulated as:

$$\rho(r) = \frac{\rho_s}{(r/r_s)^\gamma (1 + r/r_s)^{3-\gamma}}$$

where $\gamma = 1$ gives the traditional NFW profile and $\gamma = 2$ is equivalent to a singular isothermal sphere (SIS). Another option for a three–parameter profile is the Einasto profile, inspired by the two–dimensional Sersic surface brightness profile of elliptical galaxies. Both high-resolution measurements of central stellar and gas content of low surface brightness dwarf galaxies, and high–resolution CDM simulations, tend to indicate more consistency with a three–parameter density profile rather than the traditional NFW ones. There are various studies suggesting that simulated CDM halos are better described by a three–parameter model such as the Einasto profile than the standard NFW (e.g. Navarro et al. 2004; Gao et al. 2008; Di Cintio et al. 2014; Dutton & Macciò 2014). The extra parameter describing dark halo density profiles, $\alpha_{\rm Ein}$, gives the density profile more flexibility in shape, i.e. $\gamma(r) = -d\ln\rho/d\ln r$. The three–dimensional Einasto profile takes the form:

$$\ln\left(\frac{\rho(r)}{\rho_s}\right) = -b\left[\left(\frac{r}{r_s}\right)^{\frac{1}{n}} - 1\right]$$

where the *Einasto index* $\alpha_{\rm Ein} = \frac{1}{n}$, and therefore the logarithmic slope becomes $\gamma = -\frac{b}{n}(\frac{r}{r_s})^{\frac{1}{n}}$. Best–fit density profiles to simulated dark matter halos of a variety of masses in the Aquarius project show inner slopes shallower than the original NFW (Navarro et al. 2010). These halos are not self–similar, i.e. Einasto index changes with halo mass. Navarro et al. (2004) find the Einasto index for halos in the mass range between dwarves and clusters to be 0.12–0.22, with an average value of 0.17. According to Hayashi & White (2008); Gao et al. (2008), $\alpha_{\rm Ein}$ tends to increase with mass and redshift in halos of the Millennium simulation. From the gravitational lensing point of view, Einasto profiles are more demanding to work with as one cannot derive an analytical surface mass density as a function of $\alpha_{\rm Ein}$. Hence the lens equation needs to be solved numerically for each case.
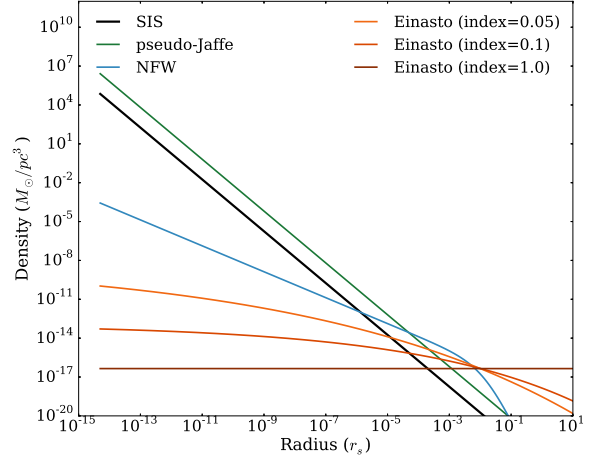
Figure 1. Four different inner density profiles of dark matter halos; Singular isothermal sphere (SIS) shown in black, the pseudo-Jaffe profile in green, the standard CDM halo profile suggested by NFW in blue, and the three–parameter Einasto profile with different Einasto indices in shades of brown. All profiles are normalized to the virial subhalo mass $M_{\rm vir} = 10^8 M_\odot$, and the Bullock et al. (2001) recipe is adopted to set the concentration parameter $c_{\rm vir}$ at $z = 0.5$. A range of about two decades in Einasto indices show that investigating $\alpha_{\rm Ein}$ in a range between $10^{-2} - 10^{-1}$ is in principle relevant in the context of gravitational lensing. Note must be taken that the Einasto index depends systematically on mass, meaning that the term "universal" density profile needs to be used having that in mind that density profiles of halos with various masses are not self–similar.

3 METHOD

The Einstein radii of lens perturbers with $\rho(r) \propto r^{-2}$ (SIS or pseudo–Jaffe profiles) and virial masses corresponding to the dark matter substructure mass range $M_{\rm vir} < 10^{10} M_\odot$ is over an order of magnitude too small to be directly detectable even with milliarcsecond resolution (see Figure 1 in Riehm et al. 2008). However, as a result of the shear made by the lens perturber, corresponding surface brightness perturbations appear at a range of angular scales larger than R_E.

The lensing simulations we present here employ Glafic, a grid–based software which solves the gravitational lensing equation employing several lens and source models (Oguri, Inoue, & Minowa 2010). A high–resolution source surface brightness model based on generic properties of sub–mm galaxies (see section 3.1) goes into the lensing code, where various lens systems – as discussed in section 4 – are tested for a single source model. The simulated image of the lensed SMG is then fed into the CASA simulator as the sky model where expected visibility measurements of ALMA are calculated based on observational settings as detailed in 3.2. The background cosmology throughout the work is a flat ΛCDM model where $\Omega_m = 0.27$, and $H_0 = 100h$ km s^{-1} Mpc^{-1} and $h = 0.7$.

The raw visibilities from CASA are then weighted, once to optimize the resulting angular resolution -in cost of sensitivity- and once for the most sensitivity, sacrificing the angular resolution. When comparing simulated observations with models, the χ^2 is simultaneously minimized for

the two weighting schemes. Therefore, the best–fit model is only achieved when the simulated data fits the model in both short– and long–spacings, i.e. large and small angular scales respectively. When the focus is on the subhalo mass resolution (section 4.1), our emphasis is on steep inner density profiles (singular isothermal spheres (SIS) and pseudo–Jaffe profiles). In cases where we focus on the inner density profiles of the substructure (section 4.2), the shallower density profile models (NFW and Einasto) are considered. This is due to the poor detection prospects for standard subhalos of the relevant mass range with this technique (see figure 4).

One interesting question to answer is, what is the minimum mass for a lens perturber (of any inner density profile) to be detectable from a smooth lens. This question addresses the mere presence of dark subhalos within the main halo. The mass detection limit for SIS and pseudo–Jaffe profiles gives a comparison between the results of this method and others. However, unlike these compact density profiles, CDM halo substructures are better represented by the three–parameter profiles, NFW, and Einasto. Without a handle on both mass and density profile of the detected subhalo, neither of the physical parameters related to the CDM model – subhalo mass function slope and the fraction of mass within a galaxy–sized halo in the form of dark substructures – are addressed. While detecting the gravitational lensing effect of a subhalo within the main halo is relatively straightforward, deriving the physical mass from gravitational lensing observations is not (see section 5 for a more detailed discussion). Therefore, in case of CDM subhalo density profiles, we investigate the degeneracy between the mass and the shape parameter α_{Ein}.

3.1 Strongly–lensed sources

There are a few criteria to fulfill when searching for strongly–lensed targets suitable for millilensing by halo substructures. One is the achievable angular resolution and the other the covered area in the lens plane probing the potential substructures of the lens. Optimizing the combination of the two leads to different combinations of source and observing frequency which are limited by the instrumental capabilities. A previous work by Zackrisson et al. (2013) investigates the prospects of halo substructure detection using synchrotron emission by blazars observable at high angular resolutions by various VLBI arrays at frequencies between $8.4 - 86$ GHz. However, the synchrotron radiation from blazars is emitted within compact regions much smaller than a parsec, while a star–forming galaxy emits thermal dust continuum across a physical region a few orders of magnitude more extended. As concluded in Zackrisson et al. (2013), in addition to very high angular resolution observations for both standard CDM halos and compact alternative substructures, larger covering of the lens plane is needed to boost the probability of suitable lens–source alignment to sample even the massive end of the subhalo mass function. This work employs simulations of continuum emission from multiply–lensed sub–mm galaxies (SMGs) to investigate the prospects of detecting and constraining the inner density slope of dark halo substructures. Sub–millimeter galaxies have a redshift distribution which peaks at $z \simeq 2$ (Wardlow et al. 2013) and typical flux densities of $S_{850} \geq 5$ mJy (Karim et al. 2013). The study of lensed SMGs with angular resolution of the order ~ 0.1 mas

can provide spatial resolutions of a few 100 pc in the source plane, at $z \sim 2$, which in turn corresponds to a spatial resolution of a few $\times$ 10 pc in the lens plane at $z \sim 0.5$. This is sufficient to probe dwarf galaxies and dark substructure of the galactic halo. The percentage of SMGs expected to be strongly–lensed with an average magnification factor of $\mu \sim 9$ is 32–74% (for $S_{500\mu m} \geq 100$ mJy) and 15–40% (for $S_{500\mu m}$ between 80-100 mJy) (Wardlow et al. 2013).

Blain et al. (1999) compare the unlensed SMG number counts at 450 and 850 μm – roughly corresponding to ALMA band 9, and band 7, respectively. Although the observed points are scarce, the population model suggests more numerous sources of the same flux density at 850 μm, while those detected at 450μm window are fewer but more luminous. In the context of strong (galaxy–galaxy) lensing, this implies better chances of suitable strong lensing alignments at lower frequency bands. This, beside the results presented in section 4 makes ALMA band 7 and 8 observations preferred over those of band 9 in the for the purpose of this work.

3.2 Lensing simulations

To simulate the effects of dark halo substructure on macrolensed SMGs, we use a numerical scheme similar to that developed by Metcalf & Madau (2001), and the illustration in figure 2. An extended source is assumed to be multiply–imaged by a foreground galaxy, and the lens equation is used to determine the lens plane positions of the corresponding macroimages. A lens perturber (substructure) is then placed along the line of sight to one of the macroimages. The deflection angles (with contributions both from the subhalo and the macrolens) are computed for every pixel within this region and converted into a numerical surface brightness map of the macroimage. These maps are initially generated with a very fine pixel scale, but are then run through CASA to create the expected visibilities achieved with ALMA in the most extended configuration. This extended configuration has a maximum baseline $\simeq 16$ km and provides an angular resolution between $7 - 10$ mas depending on the observational frequency band (band 7: $275 - 370$ GHz, band 8: $385 - 500$ GHz, and band 9: $602 - 720$ GHz).

Sizes of SMGs are between 4–8 kpc (Swinbank et al. 2008). We model the dust continuum emission with a single Gaussian component with FWHM $\simeq 0.5 - 1.0$ arcsec and an unlensed flux density of 5 mJy at $z = 2.0$. Additional surface brightness structure in the galaxy due to the distribution of star forming regions will increase the lensing effect. Given the relatively strong continuum emission from these sources the required integration time with the full array does not exceed 2 hours.

The lens model has 19 independent parameters for the source (7), main lens(7), and the lens perturber, aka. subhalo (5) as listed:

Source : Position relative to the center of the observed emission ($\Delta\alpha_s$ and $\Delta\delta_s$), the intrinsic flux density (F_s), the half–light radius (r_s), ellipticity (ϵ_s), position angle (ϕ_s), and the redshift (z_s).

Main lens The main lens is assumed to be a singular isothermal sphere, a commonly–used model for an early–

type galaxies (e.g. Rusin, Kochanek, & Keeton (2003); Keeton (2003); & Koopmans et al. (2006)). The mass of the main lens is set by the corresponding line–of–sight velocity dispersion (σ_l), position ($\Delta\alpha_l$ and $\Delta\delta_l$), ellipticity and position angle (ϵ_l, and ϕ_l), the core radius (r_l^c), and the redshift (z_l).

Lens perturber The inner density profile of the lens perturber, i.e. dark substructure, is parameterized in the lens model with the combination of a concentration parameter ($c_{\rm sub}$), and the Einasto index ($\alpha_{\rm Ein}$). The two are additional parameters to any assumed lens. All perturbers are assumed spherically symmetric, i.e. ellipticity and position angle ($\epsilon_{\rm sub}$, and $\phi_{\rm sub}$) equal zero, and in the lens plane, i.e. $z_{\rm sub} = z_l$. Even though no multi–plane lens modeling has been performed, the effect of line–of–sight contamination is briefly discussed in the discussion section (section 5).

Simulations presented in this paper are all based on a lens–source configuration that in the absence of substructure would give typical magnifications $\mu_1 \approx 10$ for at least one of the macroimages. This is consistent with typical magnification for observed SMGs (e.g. Wardlow et al. 2013). For each system, a lens configuration with $\mu \simeq 10$ is chosen to ensure a macrolens magnification that is not unrealistically high. The substructure is placed to be projected in a radius of ~ 1 mas away from the image in the system with a magnification ~ 10.

An overview of the model surface brightnesses are illustrated in the first two rows in figure 3. The contour lines on all subframes show the main lens model (without substructure) down to 10% of the maximum flux density and the color map on each frame indicates the effect of a substructure (with different inner density profile in the different subframes) on the surface brightness distribution of the lensed source. The following rows are CASA simulations imaged using *natural* and *uniform* weighting, respectively. By comparing the corresponding subfigures in each set one can spot the differences in lensing residuals due to various weighting schemes. One relevant feature seen already in the lensing models is the clear presence of a small–scale perturbation at the position of the substructure when the substructure is in the form of compact halos (SIS and pseudo–Jaffe). On the other hand, the Einasto ($\alpha_{\rm Ein} = 0.05$) substructure shows the most significant large–scale perturbation among all other substructures, both in the lensing model and in the *normal*ly–weighted images, but much less significantly on the images made using uniform weighting scheme.

The color map is normalized by the peak flux density in the smooth lens model, and measures the difference in flux density of the smooth lens and the perturbed lens system. The flux residuals in ranges of $f_{\rm res} \leq -0.1$ and $f_{\rm res} \geq 0.1$, marking 10% of the peak are marked as significant. While most of the effects are concentrated around peaks of the marcoimage, in stronger cases, the large scale differences are present at detectable levels. In case of compact lens perturbers, SIS and pseudo–Jaffe, clearly detectable small–scale effects are also present (strong blue spots on the upper right macroimage). In principle, this small–scale effect is present in all lensing case, but remains below the resolution limit for others.

3.3 Visibility modeling

In radio interferometry, the direct measured sky values are complex visibilities measured at various (u,v) distances. Each visibility point carries information about flux from all over the sky. As a result of the Fourier transformation, narrow features on the (u,v) plane transform into wide features on the image plane and vice–versa. Therefore, surface brightness maps (images) made of interferometry data are subject to various assumptions in the deconvolution step. The resulting images of the same visibility set can differ notably in featured structures. These differences depend on the prior knowledge of the user about the source, and the chosen weighting scheme. In other words, pixel–to–pixel errors on the image plane are correlated and affected by the choice of grid cells in the imaging process. Therefore, direct visibility modeling is favored over surface brightness map model comparison. In simple cases where the source could be reduced into simple analytical components, e.g. a point source, Gaussian profile, uniform disk, circular ring, etc., or a combination of them, the best fit visibility model could be found by surveying the parameter space of each component. If the flux density distribution of the source in the image plane is more complicated, however, initially a flux density distribution in the image plane is made and then the calculated visibilities of that is compared to observed values. This method requires calculating the visibilities of all investigated points in the parameter space, and fitting measured visibilities to those of the models, and therefore is more computationally involved than image plane modeling.

To account for lensing effects on both large and small angular scales, the commonly–used *natural* and *uniform* weighting schemes are used simultaneously to fit the visibilities. Even by changing the weighting scheme, in order to do a pixel–to–pixel comparison, the (u,v) plane cell size needs to remain unchanged. For fulfilling the criterion of Nyquist sampling, $\Delta x < \frac{1}{u_{\rm max}}$, the minimum (u,v) grid sizes for band 7, 8, and 9 are ~ 0.006, ~ 0.005, and ~ 0.002 respectively. In all cases, an integration time of ≤ 6 s is adopted to avoid information loss in phases, given that the luminous ring is about an arcsecond away from the phase center.

(u,v) sampling tends to be denser near the origin of the (u,v) plane, giving a better signal to noise ratio for short–spacing measurements. Normal beam convolution corresponds to a sampling/weighting function in the (u,v) plane that is usually depending on the radial distance from the origin on the (u,v,) plane. Therefore, giving all datapoints the same weight (as in the *natural* weighting scheme), leaves the relative contribution of data to the sampling function. With the emphasis on short–spacings, the thermal rms noise level of the resulting map gets minimized, as the synthesized beam gets broader. This means that the small–scale structure of the source gets washed out by beam convolution and is an undesirable effect for a composite source. The alternatives, for preserving most of the structure in the source, at the cost of sensitivity, is to either set a minimum (u,v) limit, or downweight the datasets close to the origin on the (u,v) plane. The other commonly–used weighting scheme, known as *uniform* weighting is simply designed to weight visibilities at various (u,v) distances inversely proportional to their abundance. The detail of weighting in this scheme
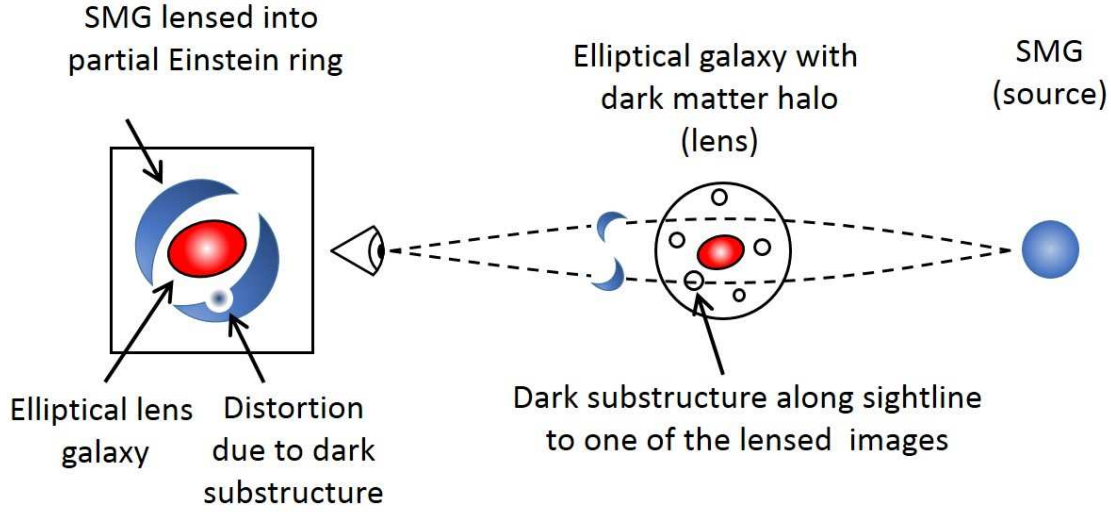
Figure 2. A schematic view of the spacial setup of the lens system. The source (sub–mm galaxy at $z \simeq 2$) is multiply–imaged by the main lens. If the dark matter halo of the lens galaxy is populated with substructures, a subhalo along the line of sight towards one of the macroimages causes a secondary lensing effect. Given a strong–enough secondary lensing due to the subhalo, this distortion will only affect one of the macroimages, while the others remain intact, unlike any source structure that replicates in all macroimages.

depends on griding of the (u,v) plane, where each data point is weighted according to

$$w_k = \frac{1}{N_s(k)}$$

where $N_s(k)$ is the number of data points within a symmetric region (cell) around the kth data point on the (u,v) plane. The visibility plane is usually gridded into regularly–spaced square cells to ease the use of FFT algorithms. However, since data points are not regularly–spaced in the visibility plane, an interpolation operation is required.

The same weighting recipes as in CASA `clean` task are applied to simulated visibilities on the visibility plane. *Natural* weighting scheme which simply weights visibilities inversely proportional to the variance of their distribution. Therefore, short–Šspacings in the (u,v) plane, with closer samplings, are weighted more than longer baselines which results in higher dynamic range in the modeled image at the cost of a coarser angular resolution. In other words, the dirty beam has larger FWHM, but less prominent side lobes. Using natural weighting scheme, therefore, places a conservative assumption on the angular resolutions discussed in this work. *Uniform* weighting scheme, on the other hand, increases the contribution from long–spacings and therefore results in a dirty beam with narrower FWHM, i.e. higher angular resolution, at the cost of increasing the resulting rms noise on the image plane. The narrower beam, therefore, can pick up small–scale structures that are smeared out by the beam in the naturally weighted image/visibility.

To find the effect of the projected subhalo, the smooth lens model is subtracted from the measurement set. The smooth lens model is assumed well–constrained. Therefore,

the remaining emission is due to the presence of a perturber in the lens. Any difference in the magnification map of an individual perturber with respect to another, will result in a different visibility residual making the two lens perturbers distinguishable.

Simulated ALMA visibilities are made using CASA software and the atmospheric thermal noise available in CASA through setting `thermalnoise="tsys-atm"` in `simobserve` is used as the noise estimate. Initially samples are drawn from the substructure parameter domain as inputs to the lensing software. The corresponding surface brightness then is sent into CASA to calculate complex visibilities. In each case a substructure of a random mass is projected within an area of 1 mas radius away from the image. The parameter space for the projected substructure covers the mass range of $M_{sub} = 3 \times 10^5 - 3 \times 10^{11} M_\odot$ and the Einasto index of $\alpha_{Ein} = 0.05 - 0.4$, as well as fixed instances of other density profiles; SIS, pseudo–Jaffe, NFW and truncated NFW. The best–fit model to the visibilities of each instance is then derived by minimizing the χ^2 of the visibilities of the simulated data set with the model visibility simultaneously for the two weighting scheme. Therefore, the best–fit model is chosen by minimizing

$$\chi^2 = \chi^2_{uniform} + \chi^2_{natural} \tag{1}$$

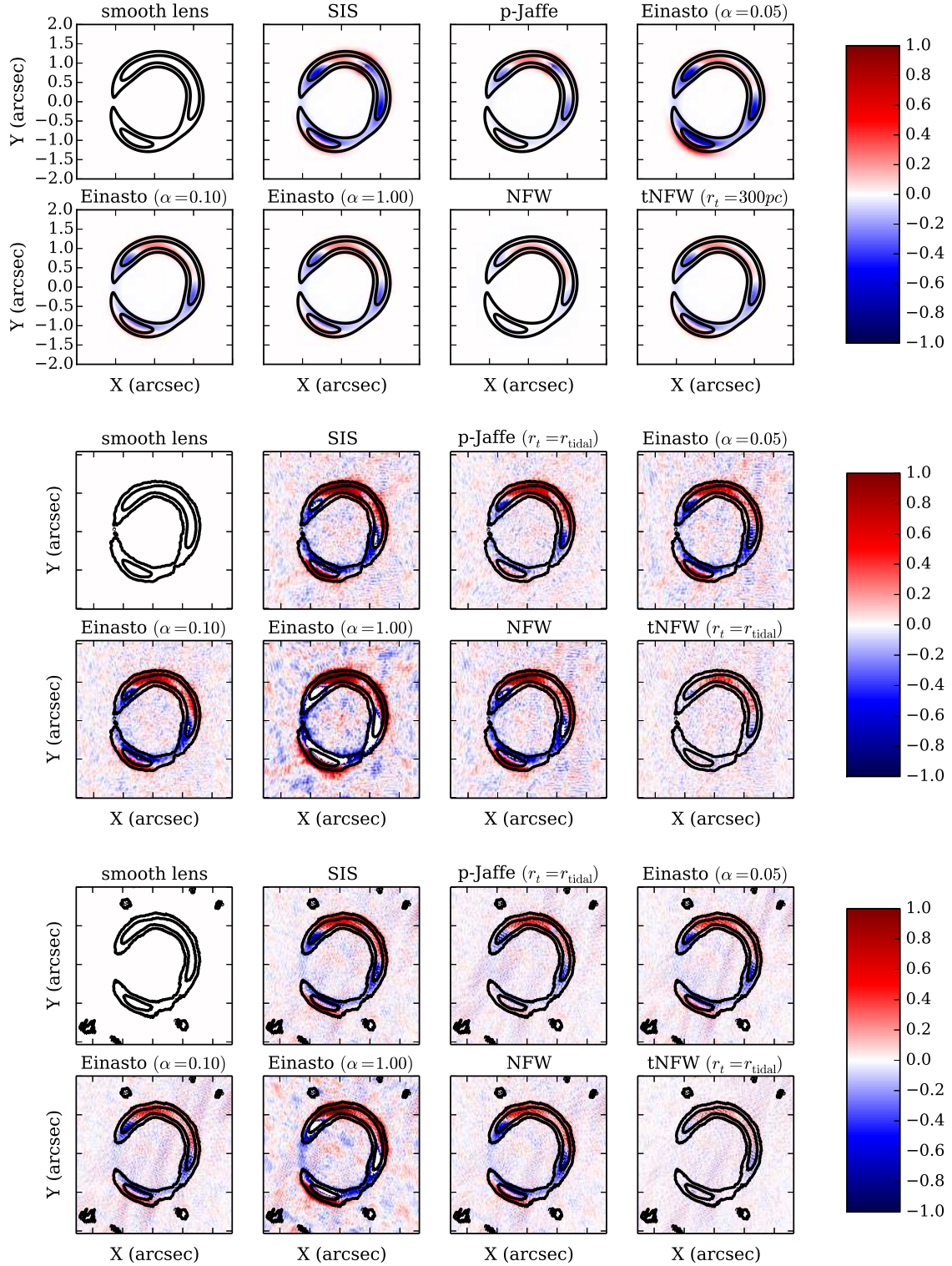Where the χ^2 for each weighting scheme is calculated using

Figure 3. Upper left frame shows a sample smooth lens system in a flux density range down to 10% of the peak. The contour plots of the following frames show the smooth system as a frame of reference for comparison while the colored maps are indicative of the residual surface brightness as a result of the presence of halo substructure compared to the smooth lens model.

the function below.

$$
\begin{aligned}
\chi^2_{\text{Real}} &= \sum_{u,v} \frac{[Re(V_{\text{smooth}}(u,v)) - Re(V_{\text{pert.}}(u,v))]^2}{\sigma^2_{\text{Real}} + \sigma^2_{\text{Imag.}}} \\
\chi^2_{\text{Imag.}} &= \sum_{u,v} \frac{[Im(V_{\text{smooth}}(u,v)) - Im(V_{\text{pert.}}(u,v))]^2}{\sigma^2_{\text{Real}} + \sigma^2_{\text{Imag.}}} \\
\chi^2 &= \chi^2_{\text{Real}} + \chi^2_{\text{Imag.}}
\end{aligned}
\tag{2}
$$

σ is the uncertainty in each visibility measurement.

Given the number of simulated data points for each set ($N_{\text{vis}} \sim 10^5 - 10^6$), the fitting process is expensive. Therefore, the explored grid is chosen to be as coarse as $\Delta\alpha_{\text{Ein}} = 0.1$ where the parameter for dark matter subhalos is weakly constrained by previous attempts and a strong degeneracy with mass is expected. The finer grid along the Einasto index is used for the next step as no significant best–fit model was found for instances with $\alpha_{\text{Ein}} > 0.4$. The final domain of investigation of the Einasto index is α_{Ein} : $[0.05, 0.40]$ with a factor of 2 increase in the parameter resolution, i.e. $\Delta\alpha_{\text{Ein}} = 0.05$.

4   RESULTS

In order to constrain the mass and inner density profile of a lens perturber (subhalo), we first assume a fixed density profile for the subhalo and investigate the detection probabilities with respect to a smooth (unperturbed) lens model by varying the mass of the perturber. The results of this part, presented in figure 4, demonstrate the comparison of the compact density profiles (SIS and pseudo–Jaffe) with the standard subhalos (NFW and tNFW) as well as the difference between field ($R_{\text{trunc}} = R_{\text{virial}}$) halos and substructures ($R_{\text{trunc}} = R_{\text{tidal}}$) of the same mass.

4.1   Mass detection limit for fixed density profiles

Cuspy, two-parameter, density profiles such as SIS and pseudo-Jaffe are not well–supported by either observational fits to central density profiles of dwarf galaxies (see e.g. Flores & Primack 1994; Moore 1994; Strigari et al. 2006; Walker et al. 2009; Boylan-Kolchin, Bullock, & Kaplinghat 2011; Amorisco, Agnello, & Evans 2013; Collins et al. 2014), or simulated subhalos, which are, as discussed in section 2 best described by the Einasto profile with the shape parameter α_{Ein} as the fitting parameter. However, to follow the common practice (see e.g. Metcalf & Madau 2001; Metcalf 2002; Vegetti et al. 2010, 2012; Hezaveh et al. 2013) in gravitational lens modeling to fit SIS or pseudo–Jaffe to the lens substructure, we here report the mass detection limit given by our method for these density profiles as well. Figure 4 illustrates the detection significance of SIS perturbers of various M_{vir} (solid lines) compared to that of standard NFW substructures (dashed lines) as well as the tidally–truncated profiles of the two groups (pseudo–Jaffe and tNFW) with tidal radii calculated according to
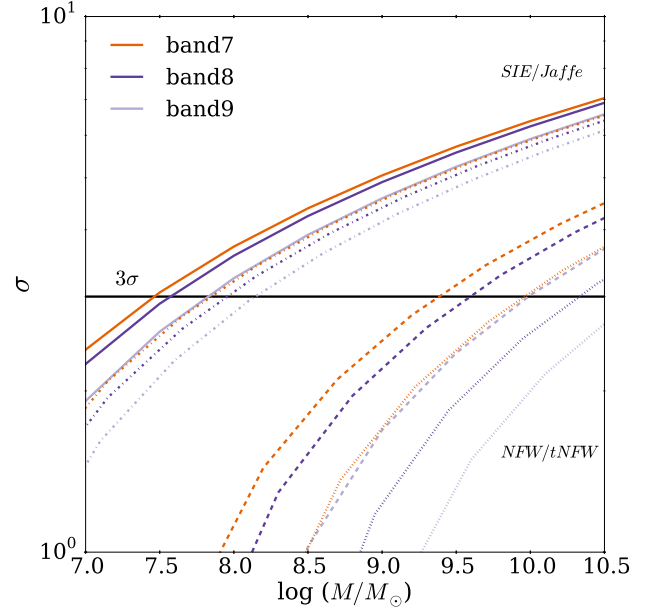

Figure 4. Comparison between the detection significance of SIS (solid lines), pseudo–Jaffe (dotted dashed lines), NFW (dashed lines), and tNFW perturbers (dotted lines) with respect to a smooth lens system. The x–axis is the detection threshold in terms of substructure mass and the y–axis depicts the significance of the statistical test preferring a model with a lens perturber of the corresponding mass to the system with the main lens only for ALMA band 7 (orange), band 8 (blue) and band 9(purple). The results shown in this figure use the combination of *natural*ly– and *uniform*ly– weighted visibilities for each frequency band.

(Tormen, Diaferio, & Syer 1998) and in agreement with Springel et al. (2008)as below:

$$
r_t = (M_{\text{sub}}/([2 - \frac{dlnM}{dlnr}]M(<r)))^{1/3}r
\tag{3}
$$

where $M(<r)$ is the host halo mass within radius r.

The illustrated detection significance is derived from modeling simulated ALMA observations in shown bands, and illustrates the substructure mass limit at which the perturbed model gives a significantly better fit to the simulated visibilities than the smooth lens model. Setting the significance level at a 3σ detection of the substructure in the system, the smallest detectable SIS subhalo mass varies between $3 \times 10^7 M_{\odot}$ for band 7 to $5 \times 10^7 M_{\odot}$ for band 8, and $8 \times 10^7 M_{\odot}$ for band 9. The same mass detection result is shown for standard NFW substructures (dashed lines in Figure 4). The much higher mass detection limits (more than 2 subhalo mass decades) for NFW halos compared to that of SIS profiles, place the detected NFW subhalos barely in the mass range relevant for galaxy subhalos, i.e. $M_{\text{vir}} \sim 10^5 - 10^{10} M_{\odot}$.

Subhalo profiles with shallower central density slopes, even when contain masses as high as $10^{11} M_{\odot}$, add only large–scale perturbation to the main lens, i.e. astrometric shifts. Lensing effects of these subhalos therefore are more pronounced in *natural*ly–weighted images. In other words, what

is needed is mostly increased sensitivity of observational data, rather than angular resolution. The local (pixel-by-pixel comparison) surface brightness perturbation for these halos (when $M \leq 10^{10} M_\odot$) does not exceed more than 1 in 100 compared to the smooth model. Even though the accumulated surface brightness perturbation between a smooth and a perturbed model reaches 0.1 of the original, it remains degenerate with the external shear. Therefore, these density profiles are only reconstructible when the external shear of the len system is known.

In the absence of any detectable local perturbation made by subhalo profiles, and consistent with the analysis above, the original NFW halos (gNFW) are more efficient in producing astrometric shifts compared to the smooth lens model than the more physically-sound tidally-truncated subhalos (tNFW) as the latter lacks the extended tail in the the density profile of former halos which is the key to the astrometric shifts.

When it comes to the more compact halos (SIS and pseudo–jaffe), the flux perturbation is more concentrated on small–scale effects; making the detectability more dependable on the angular resolution of the observational data rather than the sensitivity. If the subhalo happens to be projected close to one of the point lens images, sensitivity limit plays no role in the detectability of the subhalo. At the same time, because of the dominance of the local effects, the detectability limits depend more on the exact position of the subhalo with respect to the macroimage, as well as the local flux gradient of the image. Therefore, in the absence of other highly–magnified macroimages, the subhalo flux perturbation becomes indistinguishable from the potential structure of the source. In comparing the detectability limits for the SIS and the pseudo–jaffe profiles, the same analysis as in the case of original vs. tidally–truncated NFW works, such that the SIS subhalo gives rise to more astrometric shift than a pseudo–jaffe profile of the same mass due to the more extended tail of the density profile. The local effects of the two density profiles are, however, identical and because the detectability mass limits are lower for these halos, the astrometric shifts made by SIS halos are below the sensitivity limit of the [simulated] observations.

4.2 Mass–concentration degeneracy

The second part of our study concerns breaking the degeneracy between the mass and the concentration parameter of the perturber. In this part, a parameter space covering a range of subhalo masses between $10^5 M_\odot$ and $10^{11} M_\odot$ and the shape parameter $\alpha_{\rm Ein}$ is searched for the best–fit model to simulated data and we are comparing the detectability of 3–parameter substructures with different shape parameters $\alpha_{\rm Ein}$.

Since the detection mass limit of the NFW substructures is on the massive side for galactic subhalos when both the density profile of the subhalo and the virial mass are set as fitting parameters, in this section we are comparing lens systems with Einasto perturbers of same masses but various shape parameters with each other. In other words, the mere presence of a lens perturber in the system is assumed and the flux density perturbations due to the differences in the shape parameter of the Einasto perturber is sought. The line width in figure 5 shows the significance with which the
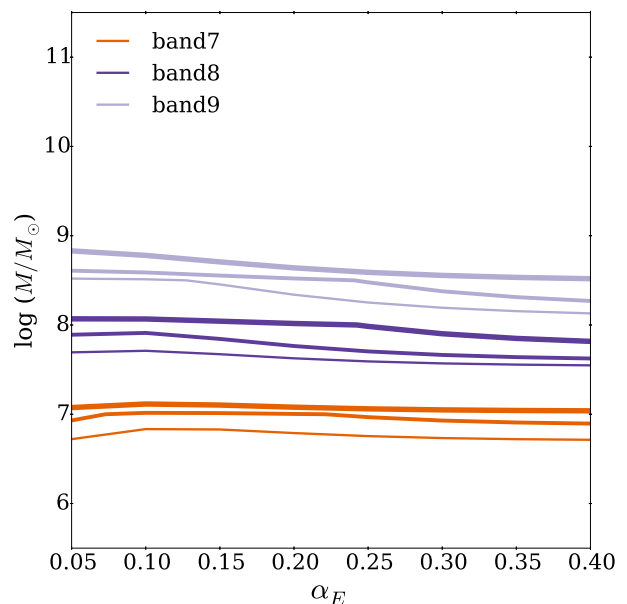
Figure 5. Comparing detection significance for Einasto profiles within a range of masses and Einasto indices. Different line colors are representative of the results given simulated observations with 3 different frequency bands of ALMA. Line widths correspond to the detection significance of the model with the given $M_{\rm Einasto}$ and $\alpha_{\rm Ein}$ with respect to that of a smooth lens model.

Einasto profile is distinguishable from the SIS of the same mass. However, the lensing signal of the substructure is so weakly depending on the shape parameter that the mass and shape parameter of the Einasto profile remains degenerate within 5 decades of subhalo mass.

5 DISCUSSION

5.1 Substructure mass estimation

In this section we argue that comparison between the mass within the Einstein radius of the lens, derived directly from solving the lensing equation, and the physical mass of the lens, i.e. the tidal subhalo mass as discussed in N–body simulations, strongly depends on the assumptions about both the density profile and truncation radius of the halo.

Conventionally, simulated subhalo mass is presented as $M_{\rm tidal}$, while the dwarf galaxy total/integrated mass is described within the central 300 pc as M_{300}. When discussing the detection limit of dark subhalos via gravitational lensing in the context of galaxy formation, it is crucial to make sure that the subhalo mass definitions assumed in lens modelings and N–body simulations are properly converted. This issue can be reduced to two different interpretations of the truncation radius of the halo, which becomes especially important when it comes to low–mass halos where detailed lensing signals are strongly affected by inner density slope and concentration (Zackrisson et al. 2008).

Einstein radius is defined as the radius within which, the mean surface mass density of the lens is equal to the
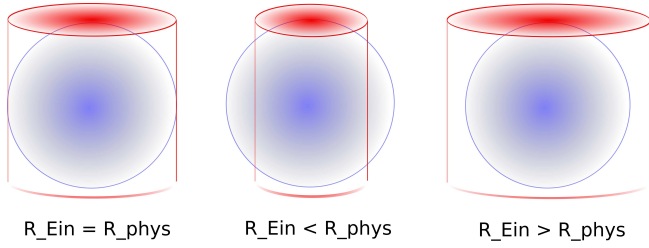
R_Ein = R_phys   R_Ein < R_phys   R_Ein > R_phys

Figure 6. This simplified illustration shows how deriving the 3D mass of a spherical halo based on the mass measured in gravitational lensing (projected mass) could vary depending on the assumed physical radius of the halo.

critical surface mass density of the Universe at the redshift of the lens. Consequently, the Einstein mass is defined as the mass within the Einstein radius of the lens,

$$M_{\mathrm{Ein}} = \Sigma_{\mathrm{crit}} \pi R_{\mathrm{Ein}}^2$$

In a strong lens system, the Einstein radius is a direct measure of the Einstein ring, arc or image separation. However, in lens systems such as the compound systems discussed in this paper, the direct measurement of the size of the Einstein radius using image separation is limited by the angular resolution. Besides, the projected mass contributing to the surface mass density of the lens corresponds to a combination of mass components including the main lens, the lens perturber (substructure) and an external shear accounting for the remaining mass components on the lens plane or along the line of sight.

Figure 6 illustrates how the measured M_{Ein}, depends on the mass concentration within the lens as well as its physical truncation radius. In other words, the degeneracy between the Einstein mass of an observed lens and its physical 3D mass is only breakable if all fitting parameters of the model halo (M_{trunc}, R_{trunc}, M_{Ein} and R_{Ein}) are known. The illustration in figure 7 shows that when $R_{\mathrm{Ein}} < R_{\mathrm{phys}}$ (the case for virial halo of all the covered mass range), M_{Ein} derived from gravitational lensing only contains part of the physical mass content of the lens. Therefore, in order to derive the 3D mass content of the lens, one needs to assume a 3D density profile as well as a truncation radius, within which the actual mass content of the lens is meaningful.

While in cases where $R_{\mathrm{Ein}} < R_{\mathrm{trunc}}$ (the case for M_{300}), the mass distribution beyond R_{Ein} only affects the macrosolution, i.e. the positions of multiple images which are beyond the resolution limit for low–mass subhalos.

Therefore, in order to derive the 3D mass of the lens the truncation radius R_{trunc}, total mass within R_{trunc}, and the mass distribution within the lens are to be fitted simultaneously.

The results presented in section 4 deal with three dimensional substructure 3D tidal masses $\sim 10^8 M_\odot$. The corresponding mass enclosed within the Einstein radius of each halo can be seen in figure 7 indicating that using the full ALMA with 10 km maximum baseline and about 10 times better spatial resolution than discussed in Hezaveh et al. (2013) enhances the mass sensitivity by more than an order of magnitude.

5.2 Current state of dark matter substructure as lens perturbers

The state of detecting dark substructure in strong lenses depends on the desired alignment, as well as the angular resolution. The trade–off between the source size and observational resolution results in the variety of instruments available for hunting dark subhalos.

Vegetti et al. (2010, 2012), using the Hubble space telescope and the Keck telescope, report the detection of two dark substructures of $M_{\mathrm{Ein}} = 3.5 \times 10^9 M_\odot$ and $M_{\mathrm{Ein}} = 1.9 \times 10^8 M_\odot$ in two strong lens systems SDSS J0946+1006 and JVAS B1938+666. They derive the gravitational potential of the lens and the *local* residual of the potential of the perturbed system compared to that of a smooth lens model, to constrain the projected mass of the perturber. According to the authors, the masses of substructures detected in these systems correspond to $M_{300}^{\mathrm{p-Jaffe}} = 3.0 \times 10^8 M_\odot$ and $M_{300}^{\mathrm{SIS}} = 3.3 \times 10^7 M_\odot$ for the more massive substructure and $M_{300}^{\mathrm{p-Jaffe}} = 1.1 \times 10^8 M_\odot$ and $M_{300}^{\mathrm{SIS}} = 6.1 \times 10^6 M_\odot$ for the low–mass one. However, as discussed in 5.1, in order to reproduce the deprojection one requires the physical truncation mass assumed for the deprojection as well as the Einstein mass and radius.

More recently Birrer, Amara, & Refregier (2015) presented a more generic method using Monte Carlo algorithms to solve simultaneously for substructures in the lens and source plane. They reconstruct the surface brightness by finding the global minimum of the χ^2 and achieve a lens substructure resolution of $\sim 10^8 M_\odot$ within the HST data.

A more similar method to the one presented in this paper is what suggested by Hezaveh et al. (2013) to detect dark subhalos in compound lens systems using ALMA. The method uses spatially resolved spectroscopy of high excitation (CO) lines tracing cores of star–forming regions in lens systems of different alignments when a dusty star forming galaxy at $z = 2$ is lensed by a foreground galaxy halo at $z = 0.5$ containing dark halo substructures using a total of 1 hr integration time with band 7 ALMA cycle 1 (maximum baseline = 1.1 km). The detection mass limit for single subhalos in their simulations is reported to be $M_{\mathrm{Ein}} > 10^8 M_\odot$, translating to $M_{\mathrm{vir}}^{\mathrm{SIS}} = 3 \times 10^{10} M_\odot$ for a pseudo–Jaffe subhalo with, $\rho(r) \propto r^{-2}$ inner profile (Figure 7). It is worth mentioning that the standard dark matter density profiles are not considered in any of the works above making it difficult to derive the link between observations and theory.

Our method presented in section 3, improves this detection limit by about an order of magnitude. Looking at where the quality of fit for SIS and pseudo–Jaffe model comparison in the visibility plane cross the 3σ line in figure 4, shows our mass detection limit between $M_{\mathrm{vir}} \simeq 3 \times 10^7 M_\odot$ and $M_{\mathrm{vir}} \simeq 10^8 M_\odot$ (depending on the observational frequency band), translating to $M_{\mathrm{Ein}} \simeq 10^5 M_\odot$, although by assuming the full ALMA with an improved angular resolution by a factor of ~ 4 compared to that of cycle 1. The main difference of our method is using direct visibility measurements rather than the surface brightness, and combining two extreme weighting schemes. This combination allows for more sensitivity on arcsecond angular scales where more subtle surface brightness changes are due to the astrometric shift and more angular resolution around the macro images where
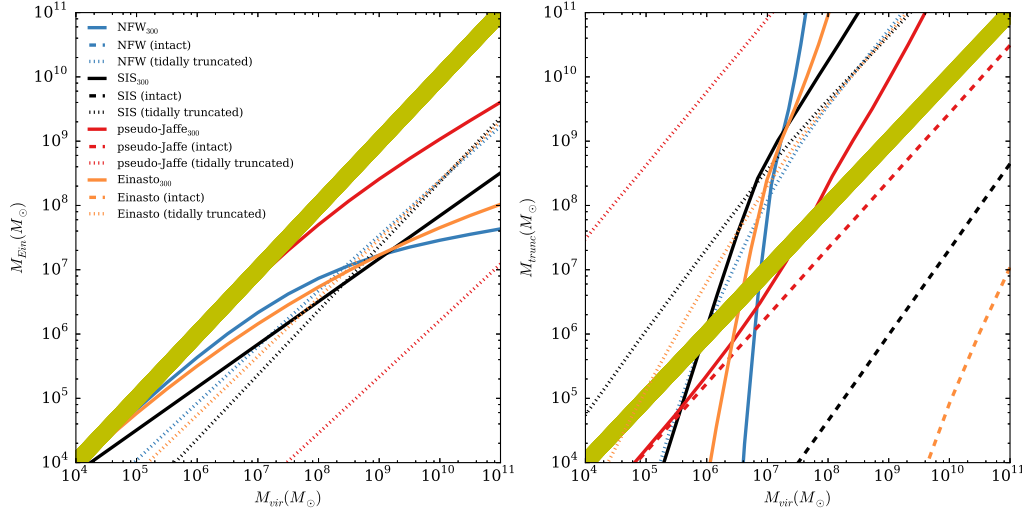
Figure 7. The importance of consistent mass conversion in comparing masses derived from lens models and N–body simulations and the effect of accounting for tidal stripping effects in outer regions of subhalos an opposed to field halos. **Left:** Translation between the virial mass and the truncated mass of halos at $z = 0.5$, for different inner density profiles. The thick yellow line has a slope of one and is therefore where all intact halos overlap. **Right:** Translation between the truncated mass and the mass within the Einstein radius of halos at $z = 0.5$, assuming $R_{trunc} = R_{Ein}$. Deviation of the mass within the half–light radius ($r_{trunc} = 300$ pc) from the virial mass is clearly visible for halos with $M_{vir} > \sim 10^6 M_\odot$ with NFW and Einasto inner density profiles while the difference tends to grow monotonously for halos with steeper logarithmic slopes, i.e. SIS and pseudo–Jaffe. One needs to keep in mind that halos with $M_{vir} \gtrsim 10^9 M_\odot$ can no longer be considered in the context of galactic substructure and consequently dwarf galaxies. The right panel shows how the mass measured within the Einstein radius deviates from the actual halo mass within the truncation radius (the virial radius for intact halos). The first immediate result is the group of dotted lines (indicating intact halos) in the lower right corner of the plot, implying large deviation of the deprojected mass within the Einstein radius from the subhalo mass within the virial radius. The red line, corresponding to pseudo–Jaffe profile shows the least deviation, while the NFW inner profile gives rise to a total Einstein mass of smaller than $10^4 M_\odot$ for subhalos with $M_{vir} \leq 10^{11} M_\odot$ consistent with expectations by comparing the central density slopes in figure 1.

there is a local magnification perturbation by the lens perturber.

5.3 Dark halos vs. luminous dwarf galaxies of the MW

Abundance matching models suggest the star formation efficiency of halos with $M_{200} < 10^{10} M_\odot$ to be smaller than 1% (Ferrero et al. 2012). This implies that only a small fraction of dark matter halos, of the same mass range as dwarf satellites, can inhabit luminous galaxies. On the other hand, the dark matter halo mass function at any given redshift is clearly predictable from the ΛCDM model (this substructure abundance, if normalized to the virial mass of the host, is independent of the host halo mass). However, observing dwarf galaxies becomes progressively more challenging as the redshift increases.

Another aspect of the comparison between the mass function of dark matter halos and the luminosity function of dwarf galaxies of the corresponding mass is the cut–off mass below which star formation inside a halo is quenched. Strigari et al. (2008) reports a common dynamical mass scale of $M_{300} \sim 10^7 M_\odot$ for a sample of SDSS dwarf satellites around the Milky Way covering a luminosity range of about four orders of magnitude. This can either imply a mass limit for dark matter halos and consequently dark matter particle mass, or for the efficiency of galaxy formation. The former issue could potentially be resolved by investigating the pres-

ence of dark matter substructures of the similar mass range, i.e. M_{Ein} between a few times $10^6 M_\odot$ to $\sim 10^9 M_\odot$ (see the right panel of figure 7).

Given a large enough sample of strong lens systems, both abundance and mass threshold of dark matter halos could be constrained. However, as discussed in section 5.1, the reliable mass translation plays a crucial role in using gravitational lensing techniques.

From a sample of 11 lensed galaxies from the SDSS at $z \simeq 0.2$, 10 null detections and one luminous dwarf galaxy as the lens perturber, in combination with a previous dark subhalo detection, Vegetti et al. (2014) infer the value for projected substructure mass fraction within the host halo in the range of $0.006 < f_{CDM} < 0.007$, consistent with the value inferred from flux–ratio anomalies (Dalal & Kochanek 2002), at $z \simeq 0.6$, but in tension with flux–ratio anomaly analysis of substructure mass between $4 \times 10^6 M_\odot$ and $4 \times 10^9 M_\odot$ by Xu et al. (2012) where they find $f_{CDM} \simeq 0.0046$. While the corresponding slope of substructure mass function by Vegetti et al. (2014), i.e. $1.90 < \alpha < 2.93$, seems to be consistent with CDM predictions, the projected mass fraction is considerably higher than that predicted by the standard CDM model ($\alpha = 1.9$ and $< f_{sub} > \sim 0.2\%$). However, the tension could be an artifact of the mass truncation issue discussed above (see figure 6). Truncated pseudo Jaffe (and even NFW) halos in the substructure mass range lie in the interesting category of $R_{Ein} < R_{phys}$, i.e. a mass deprojection leading to $M_{Ein}/M_{phys} > 1$. Therefore, different assumptions

about the physical halo could alter the derived values of f_{sub} and α. In this case, the detected halos have lower physical masses than the mass derived from their Einstein radii, resulting in a steeper inferred mass function than the actual substructure mass function. While ignoring the deprojection issue, the tension either indicates the presence of a large population of subhalos at lower redshifts contaminating the line of sight towards the lens, or other types of dark overdensities in the halo, introducing a new challenge to the standard CDM model.

5.4   low–redshift line–of–sight contamination and external shear vs. central density profile

One often–neglected correction in strong lens modeling is if the lensed image is subject to more than a single lens at a single redshift. The probability of multi–plane lensing strongly depends, among other things, on the redshift of the source. Wambsganss, Bode, & Ostriker (2004) find that in 95% of the cluster lens systems with $z_s = 1$, the secondary lens effect is negligible. While this fraction decreases steeply to 68% for systems with $z_s = 3.8$. Whether the line–of–sight contamination effects occur within the strong or weak lensing regime, precise modeling of a multi–plane lens system is impossible, because of the large number of unknown parameters. A statistical approach is, however, possible to take within the context of the background cosmology. One aspect of this correction is assuming a cosmic shear effect in addition to the simple lens model. Schneider (2014) discusses the significance of lens perturbers in intermediate redshifts on cluster lens systems, in contrast to galaxy–scale lens systems where the alignment of multiple lens planes at different redshifts is improbable, although not impossible (e.g. Chae et al. 2001; Gavazzi et al. 2008). While within the region where strong lensing occurs, accounting for the main lens gives a good approximation of the lens model, other massive objects along, or close to, the line of sight add a lensing effect that could be as strong as a few percents of that of the strong lens region. However, galaxy–galaxy lens systems with more than one deflector along the line of sight are less probable than a cluster lens system of the same redshift combination.

Therefore, results of the small–scale strong lensing effects discussed in this paper are not likely to be due to line–of–sight contamination. In an unlikely case where the substructure lensing is due to a secondary lens at a redshift different than the primary lens, this gives an estimate of the systematic error on the subhalo mass fraction and mass function derived from a statistically–meaningful sample of such detections.

6   SUMMARY

We use simulations of strong galaxy–galaxy lensing systems with ALMA band 7, 8, and 9 in search of completely dark or high mass–to–light ratio subhalos through small–scale flux density perturbations in a single lensed image. We aim for lens perturbers of $M_{sub} = 10^5 - 10^{10} M_\odot$ in a Milky Way–sized halo at $z \sim 0.5$, the relevant mass range for dark subhalos. The lensed source, i.e. the sub–mm galaxy, is at $z \sim 2.0$, a typical redshift for lensed SMGs. The analysis (comparison between the smooth and perturbed lens model) is done on

simulated complex visibilities that are weighted differently so put emphasis on different angular scales of the flux density of the source.

We show that given a single perturber within the lens system is aligned with one of the images with $\mu \approx 10$, and the presence of at least one more magnified image in the system, 1) SIS perturbers more massive than $M_{vir} \approx 3 \times 10^7 M_\odot$, $M_{vir} \approx 5 \times 10^7 M_\odot$ and $M_{vir} \approx 8 \times 10^7 M_\odot$ will be detectable with 2hr observations using ALMA band 7, band 8, and band 9, respectively. More realistic CDM density profiles (NFW and Einasto), however, are only detectable when they are more massive than a few times $10^9 M_\odot$, placing them outside the interesting mass range of dark matter substructure. 2) While observations of this kind could in principle distinguish between a compact, singular isothermal, perturber and a halo with a shallower central density profile, as described by NFW or Einasto, this method cannot break the degeneracy between the mass and the shape parameter of the perturber.

REFERENCES

Amorisco N. C., Agnello A., Evans N. W., 2013, MNRAS, 429, L89
Amorisco N. C., Evans N. W., 2012, MNRAS, 419, 184
Bennett C. L., et al., 2013, ApJS, 208, 20
Bertone G., Hooper D., Silk J., 2005, PhR, 405, 279
Birrer S., Amara A., Refregier A., 2015, arXiv, arXiv:1504.07629
Blain A. W., Smail I., Ivison R. J., Kneib J.-P., 1999, ASPC, 193, 425
Boylan-Kolchin M., Bullock J. S., Kaplinghat M., 2012, MNRAS, 422, 1203
Boylan-Kolchin M., Bullock J. S., Kaplinghat M., 2011, MNRAS, 415, L40
Bringmann T., 2009, NJPh, 11, 105027
Brooks A. M., Kuhlen M., Zolotov A., Hooper D., 2013, ApJ, 765, 22
Bullock J. S., Dekel A., Kolatt T. S., Kravtsov A. V., Klypin A. A., Porciani C., Primack J. R., 2001, ApJ, 555, 240
Chae K.-H., Turnshek D. A., Schulte-Ladbeck R. E., Rao S. M., Lupie O. L., 2001, ApJ, 561, 653
Chiba M., 2002, ApJ, 565, 17
Collins M. L. M., et al., 2014, ApJ, 783, 7
Cornell J. M., Profumo S., Shepherd W., 2013, PhRvD, 88, 015027
Cyr-Racine F.-Y., Moustakas L. A., Keeton C. R., Sigurdson K., Gilman D. A., 2015, arXiv, arXiv:1506.01724
Dalal N., Kochanek C. S., 2002, ApJ, 572, 25
de Blok W. J. G., 2010, AdAst, 2010, 789293
de Blok W. J. G., McGaugh S. S., Bosma A., Rubin V. C., 2001, ApJ, 552, L23
Del Popolo A., Lima J. A. S., Fabris J. C., Rodrigues D. C., 2014, JCAP, 4, 021
Di Cintio A., Brook C. B., Macciò A. V., Stinson G. S., Knebe A., Dutton A. A., Wadsley J., 2014, MNRAS, 437, 415
Dutton A. A., Macciò A. V., 2014, MNRAS, 441, 3359
Ferrero I., Abadi M. G., Navarro J. F., Sales L. V., Gurovich S., 2012, MNRAS, 425, 2817
Flores R. A., Primack J. R., 1994, ApJ, 427, L1

Fry A. B., et al., 2015, MNRAS, 452, 1468

Gao L., Navarro J. F., Frenk C. S., Jenkins A., Springel V., White S. D. M., 2012, MNRAS, 425, 2169

Gao L., Navarro J. F., Cole S., Frenk C. S., White S. D. M., Springel V., Jenkins A., Neto A. F., 2008, MNRAS, 387, 536

Garrison-Kimmel S., Horiuchi S., Abazajian K. N., Bullock J. S., Kaplinghat M., 2014, MNRAS, 444, 961

Gavazzi R., Treu T., Koopmans L. V. E., Bolton A. S., Moustakas L. A., Burles S., Marshall P. J., 2008, ApJ, 677, 1046

Hayashi E., White S. D. M., 2008, MNRAS, 388, 2

Hezaveh Y. D., et al., 2013, ApJ, 767, 132

Karim A., et al., 2013, MNRAS, 432, 2

Keeton C. R., 2003, ApJ, 584, 664

Klypin A., Kravtsov A. V., Valenzuela O., Prada F., 1999, ApJ, 522, 82

Kochanek C. S., Dalal N., 2004, ApJ, 610, 69

Koopmans L. V. E., Treu T., Bolton A. S., Burles S., Moustakas L. A., 2006, ApJ, 649, 599

Kuzio de Naray R., 2008, ASPC, 396, 445

Kuzio de Naray R., Spekkens K., 2011, ApJ, 741, L29

Lovell M. R., et al., 2012, MNRAS, 420, 2318

Macciò A. V., Dutton A. A., van den Bosch F. C., 2008, MNRAS, 391, 1940

Maciejewski M., Vogelsberger M., White S. D. M., Springel V., 2011, MNRAS, 415, 2475

Maxwell A. J., Wadsley J., Couchman H. M. P., 2015, ApJ, 806, 229

Metcalf R. B., 2002, ApJ, 580, 696

Metcalf R. B., Madau P., 2001, ApJ, 563, 9

Metcalf R. B., Zhao H., 2002, ApJ, 567, L5

Moore B., 1994, Natur, 370, 629

Moore B., Ghigna S., Governato F., Lake G., Quinn T., Stadel J., Tozzi P., 1999, ApJ, 524, L19

Navarro J. F., et al., 2004, MNRAS, 349, 1039

Navarro J. F., Eke V. R., Frenk C. S., 1996, MNRAS, 283, L72

Navarro J. F., Frenk C. S., White S. D. M., 1996, ApJ, 462, 563

Navarro J. F., et al., 2010, MNRAS, 402, 21

Oguri S., Inoue Y., Minowa M., 2010, NIMPA, 622, 588

Oh S.-H., Brook C., Governato F., Brinks E., Mayer L., de Blok W. J. G., Brooks A., Walter F., 2011, AJ, 142, 24

Peñarrubia J., Pontzen A., Walker M. G., Koposov S. E., 2012, ApJ, 759, L42

Planck Collaboration, et al., 2014, A&A, 571, A17

Riehm T., Zackrisson E., Möller O., Mörtsell E., Wiik K., 2008, JPhCS, 131, 012045

Rusin D., Kochanek C. S., 2005, ApJ, 623, 666

Rusin D., Kochanek C. S., Keeton C. R., 2003, ApJ, 595, 29

Sawala T., et al., 2014, arXiv, arXiv:1406.6362

Schaller M., et al., 2015, MNRAS, 451, 1247

Schneider P., 2014, arXiv, arXiv:1409.0015

Springel V., et al., 2008, MNRAS, 391, 1685

Strigari L. E., Bullock J. S., Kaplinghat M., Kravtsov A. V., Gnedin O. Y., Abazajian K., Klypin A. A., 2006, ApJ, 652, 306

Strigari L. E., Bullock J. S., Kaplinghat M., Simon J. D., Geha M., Willman B., Walker M. G., 2008, Natur, 454, 1096

Swinbank A. M., et al., 2008, MNRAS, 391, 420

Tormen G., Diaferio A., Syer D., 1998, MNRAS, 299, 728

Vegetti S., Koopmans L. V. E., Auger M. W., Treu T., Bolton A. S., 2014, MNRAS, 442, 2017

Vegetti S., Koopmans L. V. E., Bolton A., Treu T., Gavazzi R., 2010, MNRAS, 408, 1969

Vegetti S., Lagattuta D. J., McKean J. P., Auger M. W., Fassnacht C. D., Koopmans L. V. E., 2012, Natur, 481, 341

Vogelsberger M., Zavala J., Loeb A., 2012, MNRAS, 423, 3740

Walker M. G., Mateo M., Olszewski E. W., Peñarrubia J., Wyn Evans N., Gilmore G., 2009, ApJ, 704, 1274

Walker M. G., Peñarrubia J., 2011, ApJ, 742, 20

Wambsganss J., Bode P., Ostriker J. P., 2004, ApJ, 606, L93

Wang B., Justham S., Liu Z.-W., Zhang J.-J., Liu D.-D., Han Z., 2014, MNRAS, 445, 2340

Wardlow J. L., et al., 2013, ApJ, 762, 59

Wright E. L., et al., 1992, ApJ, 396, L13

Xu D. D., Mao S., Cooper A. P., Gao L., Frenk C. S., Angulo R. E., Helly J., 2012, MNRAS, 421, 2553

Xu D. D., et al., 2009, MNRAS, 398, 1235

Xu, D., Sluse, D., Gao, L., et al. 2015, MNRAS, 447, 3189

Zackrisson E., Bergvall N., Marquart T., Östlin G., 2006, A&A, 452, 857

Zackrisson E., Riehm T., Möller O., Wiik K., Nurmi P., 2008, ApJ, 684, 804

Zackrisson E., et al., 2013, MNRAS, 431, 2172

Zackrisson E., Riehm T., 2010, AdAst, 2010, 478910

Zhu Q., Marinacci F., Maji M., Li Y., Springel V., Hernquist L., 2015, arXiv, arXiv:1506.05537

This paper has been typeset from a TeX/LaTeX file prepared by the author.